Meteoritics & Planetary Science 33, 115–126 (1998)

Formation of an unusual compact Type A refractory inclusion from Allende

STEVEN B. SIMON[1]*, ANDREW M. DAVIS[2] AND LAWRENCE GROSSMAN[1,2]

[1]Department of the Geophysical Sciences, The University of Chicago, 5734 South Ellis Avenue, Chicago, Illinois 60637, USA
[2]Enrico Fermi Institute, The University of Chicago, 5640 South Ellis Avenue, Chicago, Illinois 60637, USA
*Correspondence author's e-mail address: sbs8@midway.uchicago.edu

(Received 1997 June 5; accepted in revised form 1997 October 13)

Abstract–We report the results of a study of TS2, an unusual compact Type A inclusion from Allende. A distinctive, major feature of this inclusion is that many of its melilite crystals have no dominant core-rim zoning but instead consist of 50–200 μm patches of Mg-rich melilite ($Åk_{32–62}$, median $Åk_{51}$) set in or partially enclosed by, and optically continuous with, relatively Al-rich melilite ($Åk_{25–53}$, median $Åk_{38}$). The Al-rich regions have jagged, dendritic shapes but occur within crystals having straight grain boundaries. Another unusual feature of this inclusion is the size and spatial distribution of spinel. In many places, especially in the interior of the inclusion, the aluminous melilite encloses numerous, fine (0.5–5 μm) inclusions of spinel and minor perovskite and fassaite. The latter phases also occur as isolated grains throughout the inclusion. Coarse-grained spinel, ~50–150 μm across, occurs in clumps and chains enclosed in relatively Mg-rich melilite, whereas none of the fine spinel grains are clumped together. The sample also contains a spinel-free palisade body, 1.7 × 0.85 mm, that consists almost entirely of Åk-rich (45–65 mol%) melilite. Within the palisade body are two grains of perovskite with extremely Nb-rich (~4–8 wt% Nb_2O_5) cores and rims of typical composition. All phases in this inclusion have chondrite-normalized REE patterns that are consistent with crystal/melt partitioning superimposed upon a bulk modified Group II pattern. We suggest that TS2 had an anomalous cooling history and favor the following model for the formation of TS2. Precursors having a bulk modified Group II pattern melted. Rapid growth of large, dendritic, nonstoichiometric melilite crystals occurred. The melilite trapped pockets of melt and incorporated excess spinel components and TiO_2. Bubbles formed in the residual melt. As crystallization slowed, coarse spinel grew. Some spinel grains collected against bubbles, forming spherical shells, and others formed clumps and chains. Relatively Åk-rich melilite crystallized from the residual melt between dendritic melilite crystals and from melt trapped in pockets and between arms of dendrites, and incorporated the clumps and chains of coarse spinel. Bubbles broke and filled with late-stage melt, their shapes preserved by their spinel shells. Slow cooling, or perhaps an episode of reheating, allowed the early melilite to become stoichiometric by exsolving fine grains of spinel, perovskite and fassaite, and allowed the melilite to form smooth grain boundaries. Dendritic crystals are indicative of rapid growth and the melilite crystals in TS2 appear to be dendritic. Coarse, dendritic melilite crystals have been grown from Type B inclusion melts cooled at ~50–100 °C/h. If those results are applicable to Type A inclusions, we can make the first estimate of the cooling rate of a Type A inclusion, and it is outside the range (2–50 °C/h) generally inferred for Type B inclusions. The rapid cooling inferred here may be part of an anomalous thermal history for TS2, or it may be representative of part of a normal thermal history common to Types A and B that involved rapid cooling early (at high temperatures) as inferred for TS2, and slower cooling later (at lower temperatures), as inferred for Type B inclusions. We prefer the former explanation; otherwise, the unusual features of TS2 that are reported here would be common in Type A inclusions (which they are not).

INTRODUCTION

Type A inclusions are a major type of coarse-grained refractory inclusion found in CV3 carbonaceous chondrites. First defined by Grossman (1975) as extremely melilite-rich (as opposed to pyroxene-rich) inclusions, Type A inclusions were subdivided into irregularly shaped ones and round ones by MacPherson and Grossman (1979). These two subtypes were later termed "fluffy" and "compact", respectively, by Grossman (1980). Fluffy Type A inclusions were studied by MacPherson and Grossman (1984), who concluded that they most likely formed by gas-solid condensation. Teshima and Wasserburg (1985) studied three compact Type A inclusions (CTAs) from Allende petrographically and chemically and concluded that the inclusions initially crystallized from liquids and later experienced various degrees of metamorphism that affected mineral compositions and caused "little to complete recrystallization". Beckett (1986) performed isothermal crystallization experiments on a bulk composition representing that of the inclusion considered in this paper. Perovskite-fassaite-spinel symplectites around rhönite in CTAs have been studied by Fuchs (1971), Haggerty (1976) and El Goresy *et al.* (1977). One CTA from Efremovka was thoroughly studied by Fahey *et al.* (1987). Although other CTAs have been studied, there has been no systematic study of them, and their crystallization histories are not understood in any detail. We have undertaken a study of a suite of CTAs from Allende, Axtell, and Efremovka, investigating their petrography, mineral chemistry, and trace element distributions. Preliminary results of this investigation were given by Davis *et al.* (1990) and Simon *et al.* (1995). We report here on one unique member of the suite; results for the other inclusions will be reported in a separate paper.

The subject of the current paper, Allende inclusion TS2, has the mineralogy of a typical CTA (melilite, spinel, perovskite and fassaite) with a texture, a bulk composition, and melilite zoning patterns that make it unique. We have studied this inclusion with a variety of

analytical techniques in order to obtain an understanding of how it formed. Preliminary results of this study were reported by Simon *et al.* (1997).

ANALYTICAL METHODS

A polished thin section of the inclusion was studied with a petrographic microscope. Backscattered electron (BSE) images, digital X-ray maps, and quantitative analyses were obtained with a JEOL JSM-5800 LV scanning electron microscope equipped with an Oxford/Link ISIS-300 energy-dispersive X-ray microanalysis system. Quantitative wavelength-dispersive analyses were obtained with a Cameca SX-50 electron microprobe operated at 15 kV with a beam current of 25 nA. Data were reduced *via* the modified ZAF correction procedure PAP (Pouchou and Pichoir, 1984). Trace-element analyses were obtained with the University of Chicago AEI IM-20 ion microprobe. The analytical techniques used are similar to those described in Simon *et al.* (1991) and MacPherson and Davis (1993, 1994).

RESULTS

Petrography

Inclusion TS2 is round but not quite circular in cross-section, ~6.2 × 5.8 mm. A BSE image of the inclusion, Fig. 1, shows the dominance of melilite, the sparse perovskite grains, and the clumps and chains of spinel, which were first described by Grossman (1975). Alteration products (anorthite, grossular, monticellite) are present mainly along melilite grain boundaries in the outer ~500 μm of the inclusion and in veins that extend into the interior of the inclusion. In places where veins intersect void space, wollastonite needles are abundant.

Examination in transmitted light shows that near the rim of the inclusion, melilite has uniform birefringence and occurs as equant grains ~100 μm across and as laths up to ~500 μm long, in an interlocking texture except where separated by alteration products. The abundance of the latter is evident from Fig. 1 here and Fig. 1A of Grossman (1975). In the interior of the inclusion, melilite has unusual birefringence patterns and is coarser on average than at the rim, occurring as laths up to 2 mm long with straight, serrated, or irregular grain boundaries (*i.e.*, melilite-melilite contacts).

In melilite, birefringence is strongly dependent upon Åk content. The nominal interference color of gehlenitic melilite is first-order white. Interference colors vary through gray, blue and brown with increasing Åk content. Thus, zoning patterns can be readily discerned when viewing melilite in transmitted light with crossed polarizers. In most coarse-grained inclusions, most melilite crystals have uniform or weakly zoned cores and strongly zoned rims. In many melilite crystals in TS2, however, there is no dominant core-rim zoning, but within many crystals are patches whose birefringence contrasts with that of the host crystal. An example is shown in Fig. 2, a photomicrograph taken in transmitted light with crossed polarizers, showing two melilite crystals with patchy zoning. The two grains can be distinguished by the trends of their cleavage traces. The host crystals generally have first-order white to gray interference colors, and the patches, two of which are indicated by arrows and appear dark, are typically concentrically zoned from blue (outermost edge) through reddish brown to light brown (center), reflecting increasing Åk contents toward the centers of the patches and higher Åk contents than those of the host. The patches are typically rounded, 30–50 μm across, but they can be irregular in shape and up to 200 μm across. All patches are optically continuous with their

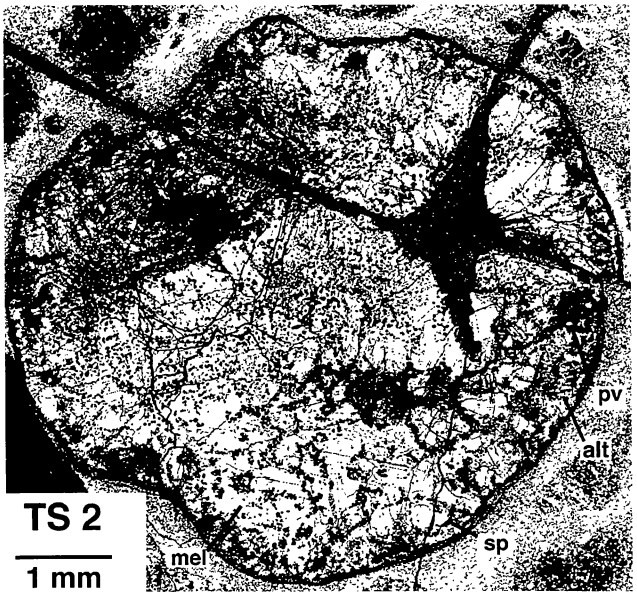

FIG. 1. Backscattered electron (BSE) image of TS2. Note rounded shape, dominance of melilite (mel), abundance of alteration products (alt) near the rim, chains of spinel (sp), and sparse perovskite (pv) grains. Large black areas are voids.

FIG. 2. Transmitted light view of two crystals of patchy melilite. Note the two cleavage directions that are approximately perpendicular to each other. Arrows indicate patches (dark) of Mg-rich melilite (~$Åk_{50}$) in relatively aluminous (~$Åk_{35}$) melilite (white). Field of view is 750 μm. Crossed polars.

hosts and do not cross grain boundaries. They do not contain spinel, but many enclose micrometer-sized, rounded grains of perovskite or fassaite.

Grossman (1975) noted that, in addition to the long chains of coarse, euhedral spinel crystals, which are visible in Fig. 1, some melilite crystals in this inclusion contain dense concentrations of fine spinel grains. This feature, which mainly occurs in melilite with patchy zoning, is best seen in BSE images, such as Fig. 3a. The fine spinels are seen here as clouds of small, black spots, especially at the top center to the upper right. As shown in Fig. 3b, the spinels range from <1 μm up to ~5 μm across and appear to be rounded. They are rarely in contact with each other but may occur adjacent to finer-grained, much less numerous inclusions of fassaite or perovskite. In contrast, the coarser spinel grains, mostly 50–150 μm across, tend to be euhedral and in contact with other spinels, either in clumps, as seen in Fig. 3a, or in chains, as seen in Fig. 1. Note also that the coarse- and fine-grained spinels are not intermingled and that clusters of coarse spinel grains tend to have spinel-free zones around them. Anhedral, rounded perovskite grains, typically ~10 μm across, commonly occur between and adjacent to coarse spinel grains, and enclosed in melilite. Both of these occurrences can be seen in Fig. 3a. Fassaite is anhedral, occurring as thin selvages on spinel grains, as very fine (<5 μm) blebs in and between melilite crystals, and as rare 10–30 μm grains enclosed in melilite.

Another distinctive feature of this inclusion is evident from the Al X-ray map (Fig. 3c) of the same area as that shown in Fig. 3a: the fine spinels occur only in the relatively aluminous melilite of the grains with patchy zoning. This image also shows that the fine spinels and aluminous melilite occur in an irregular, somewhat dendritic pattern. The relatively magnesian melilite that appears to invade the aluminous melilite, and that in patches, is either spinel-free or encloses coarse spinel. Also present in areas free of fine spinel are rare, small (~20 μm across) grains of relatively gehlenitic melilite. These grains tend to be subhedral and adjacent to coarse spinel. Like the patches of Mg-rich melilite enclosed in Mg-poor melilite, the gehlenitic grains create sharp composition contrasts. For example, in one area, just above the coarse spinel at the bottom right of Fig. 3c, very aluminous ($Åk_{13}$) and magnesian ($Åk_{68}$) melilite are only 50 μm apart.

Digital X-ray mapping of TS2 has also revealed that one of the long, curved chains of spinel marks the boundary of a palisade body. An Al X-ray map of this area (Fig. 4) shows that the palisade body is virtually spinel-free and consists of melilite that is not patchy and is more Mg-rich than the melilite that is immediately outside the boundary. The palisade body contains several large perovskite grains, ~50 μm across, that have round melilite inclusions. Two of these perovskite grains, one of which is shown in Fig. 5, have unusual, Nb-rich cores.

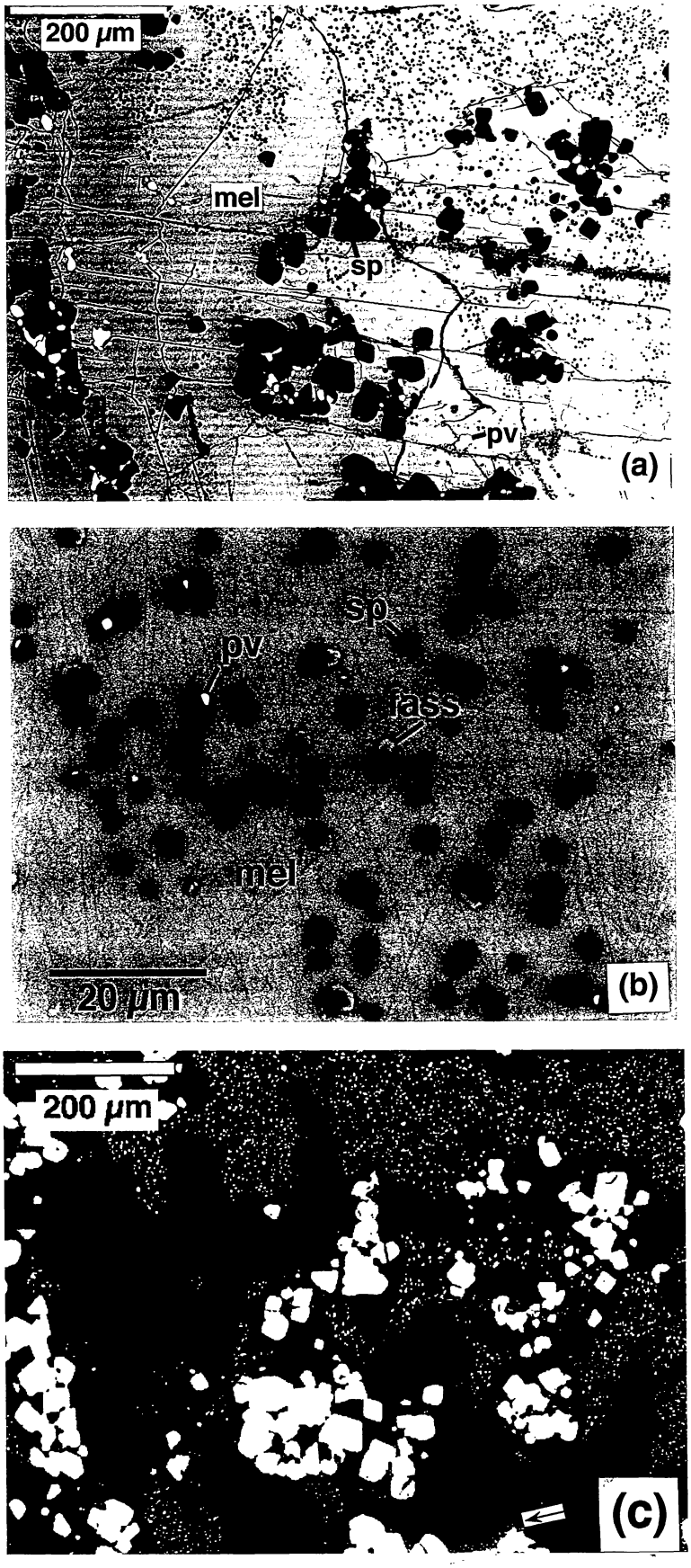

FIG. 3. (Right) Melilite crystals with patchy zoning. Note uneven distribution of spinel. (a) BSE image. (b) Close-up BSE image of area rich in fine spinel, showing the rounded grains and the occurrence of fine perovskite and fassaite. (c) Aluminum X-ray map of the area shown in (a). Note the angular, dendritic shapes of Al-rich melilite (light gray). Spinel is white. Arrow points to rare, gehlenitic melilite that is adjacent to coarse spinel. Fass: fassaite; other abbreviations as used previously.

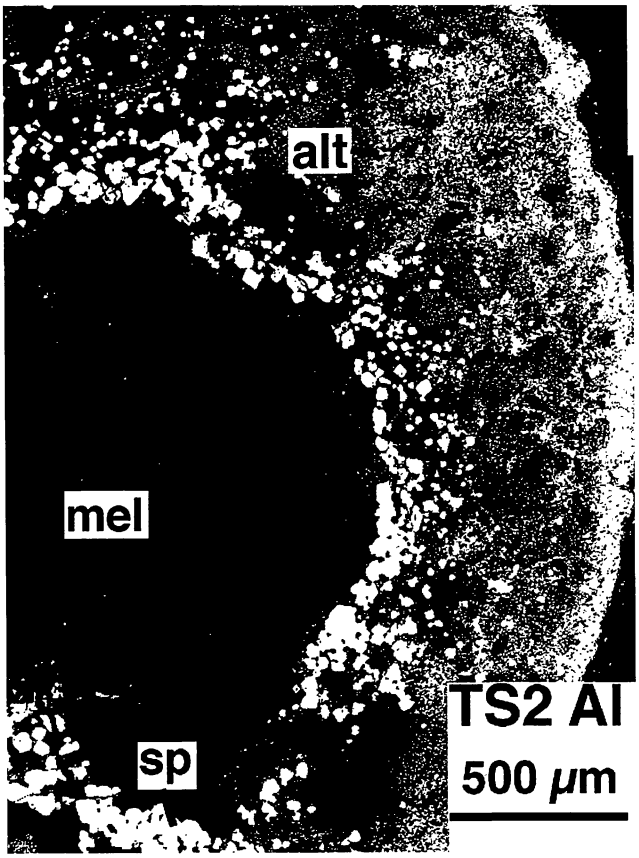

FIG. 4. Aluminum X-ray map of a portion of TS2 containing a palisade body. Melilite between the inclusion rim and the boundary of the palisade body is more aluminous than that inside the palisade body. Abbreviations as used previously.

Mineral Chemistry

Melilite–In this inclusion, melilite exhibits a wide range of compositions, from $Åk_9$ at the rim to $Åk_{68}$ in spinel-free melilite and in the palisade body. Compositions of melilite from throughout the inclusion are summarized in Fig. 6. The analyses are grouped according to petrographic setting, and they define distinct populations. Melilite from the outer ~500 μm ("Rim") of the inclusion tends to be the most aluminous, ranging from $Åk_9$ to $Åk_{55}$ with a median of $Åk_{30}$. Digital X-ray mapping and over 12 000 quantitative energy-dispersive analyses of an area of patchy melilite indicate that melilite that encloses the fine spinel is more aluminous than adjacent, spinel-free melilite. Figure 6 shows that the compositions of spinel-bearing melilite are mostly between $Åk_{25}$ and $Åk_{55}$ with a normal distribution of compositions and a median of $Åk_{38}$; whereas, the spinel-free melilite is mostly between $Åk_{30}$ and $Åk_{65}$, with a median of $Åk_{51}$ and a distribution that is skewed toward aluminous melilite. A few analyses, mainly of the small, gehlenitic grains described above, are more aluminous than $Åk_{20}$. Also shown in Fig. 6 are analyses of melilite from the palisade body, which range from $Åk_{43}$ to $Åk_{68}$ and tend to be even more magnesian than that intergrown with the aluminous melilite in the patchy areas. Four of the analyses of melilite from the palisade body are of melilite enclosed in perovskite. Three of these are within the range of the other analyses of palisade body melilite, but one, $Åk_{68}$, is outside the range.

A plot of wt% Na_2O *vs.* $X_{Åk}$ is shown in Fig. 7 for melilite from the outer ~500 μm of the inclusion, the inner patchy regions, and the palisade body. The outer melilite tends to have lower Åk and higher Na_2O contents than the patchy melilite in the interior of the inclusion. Melilite in the palisade body has higher Åk and Na_2O contents than the interior patchy melilite. A positive correlation between Na_2O and Åk contents is expected for igneous melilite because the melilite/liquid distribution coefficient (D) increases with increasing Åk content, from ~0.6 for $Åk_{33}$ to ~1 for $Åk_{50}$ and

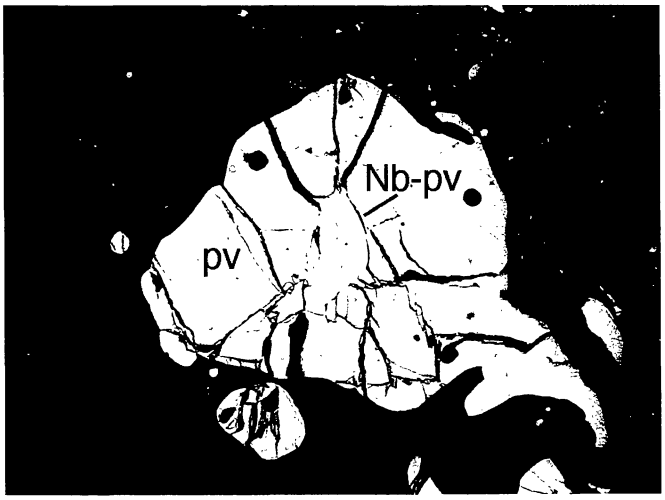

FIG. 5. Backscattered electron image of a large perovskite grain with a Nb-rich core.

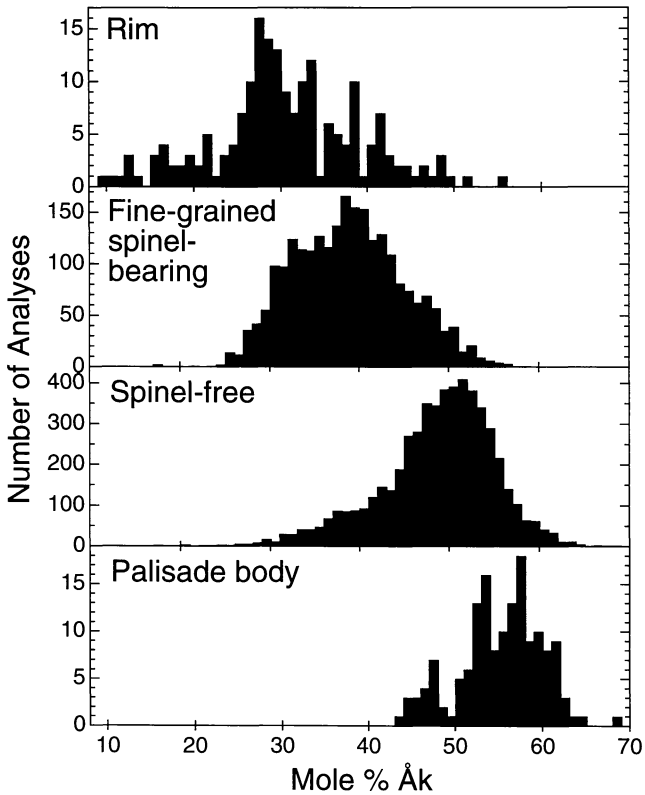

FIG. 6. Histograms of melilite compositions from various petrographic settings in TS2. Analyses of "fine-grained spinel-bearing" and "spinel-free" melilite are by energy-dispersive techniques on a scanning electron microscope; those of the palisade body and rim (outer ~500 μm) melilite are wavelength-dispersive, electron probe analyses.

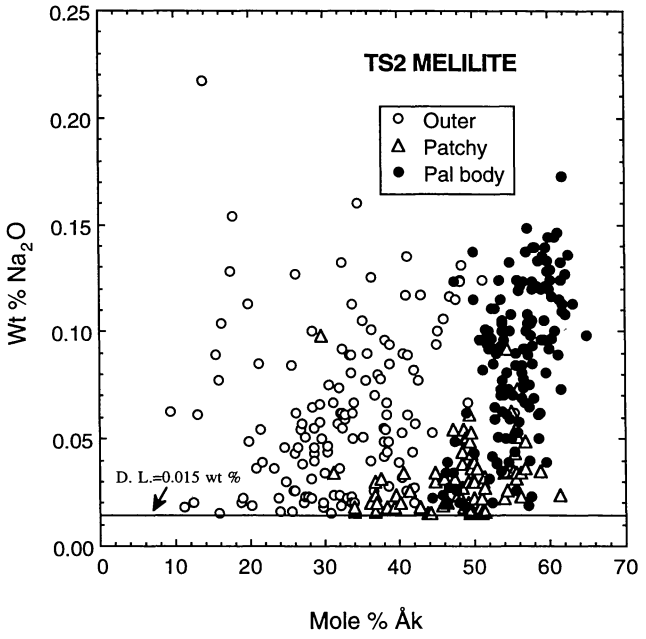

FIG. 7. Plot of wt% Na_2O *vs.* mol% Åk in melilite in TS2, determined by electron probe. D.L. = detection limit of the electron probe. Pal = palisade.

~1.5 for $Åk_{66}$ (Beckett and Stolper, 1994). Thus, if this inclusion crystallized from a liquid, it is not surprising that the (Åk-rich) melilite in the palisade body has relatively high Na_2O contents. Melilite in the outer part of the inclusion, despite its relatively low Åk contents, has Na_2O contents similar to those of the melilite in the palisade body. The high Na_2O contents of the outer melilite probably reflect late addition of alkalies to the inclusion.

Spinel–Spinel is nearly end-member $MgAl_2O_4$, with minor amounts of Cr_2O_3, V_2O_3, and TiO_2. We analyzed both coarse- and fine-grained spinel by electron probe and the results are summarized in Fig. 8. Despite the clear differences in size and occurrence between the two groups, they have rather similar compositions. The two populations overlap completely in Cr_2O_3 and TiO_2 contents, but the V_2O_3 contents of the coarse-grained spinel vary from 0.3 to 0.55 wt%; whereas, the analyses of fine spinel exhibit a narrower range, ~0.25 to 0.40 wt%. There is no correlation between composition and spatial location. Electron probe traverses across single grains, and cathodoluminescence images show that coarse spinels are unzoned.

Fassaite–Representative analyses of fassaite are given in Table 1. Fassaite in TS2 is like most previously analyzed fassaite from CTAs, with high TiO_2^{tot} (15–18 wt%) and Ti_2O_3 contents, whether in isolated grains or adjacent to spinel, and a wide range of Sc_2O_3 (from below detection, <0.044, to ~0.5 wt%) and V_2O_3 contents (from ~0.2–0.5 wt%). In contrast, fassaite in Type B inclusions generally has maxima of ~12 wt% TiO_2^{tot} and ~0.25 wt% Sc_2O_3 (Simon *et al.*, 1991). In TS2, as in Type B inclusions, fassaite tends to have lower TiO_2^{tot} contents at the rims of grains than at the cores.

Perovskite–Electron probe analyses of perovskite are given in Table 2. Analyses of niobian perovskite are given in columns 1 and 2, and "normal" perovskite, in columns 3 and 4. The niobian perovskite is also enriched in Al_2O_3, V_2O_3, and Ta_2O_5 relative to the typical perovskite in this sample. Although partitioning studies (Kennedy *et al.*, 1994) have shown that Nb is compatible in perovskite, and niobian end-member perovskites are known (*e.g.*, Mitchell, 1996), concentrations of Nb at the levels seen here (Nb/Ti ~ 350 × CI chondrites) are rare among meteoritic perovskite.

Trace Element Abundances

The ranges of the chondrite-normalized rare-earth-element (REE) patterns of each phase, determined by ion microprobe, are illustrated in Fig. 9. Representative analyses are given in Table 3. As might be expected from their crystal/liquid partition coefficients (Beckett *et al.*, 1990; Simon *et al.*, 1991; Kennedy *et al.*, 1994), the absolute abundances of the trivalent REE and Y increase in the

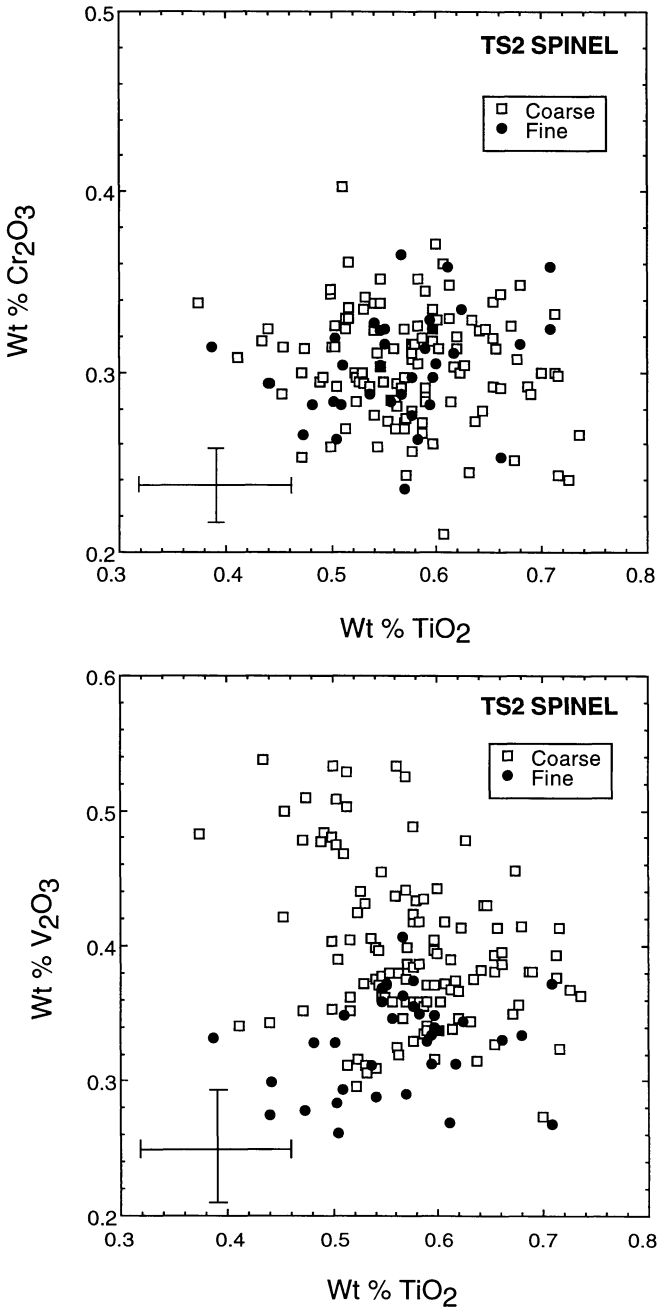

FIG. 8. Plots of V_2O_3 and Cr_2O_3 *vs.* TiO_2 in both coarse- and fine-grained spinel. Representative 2σ error bars (based on counting statistics) are shown.

order melilite, fassaite, perovskite. We can calculate a bulk REE pattern for TS2 from the phase abundances estimated from BSE images and their average REE contents. When we do so, we obtain abundances for La, Sm, Eu and Yb of 7.4, 9.5, 25, and 4.3 × CI,

TABLE 1. Electron microprobe analyses of fassaite in TS2.

	1	2	3	4	5
MgO	8.18	7.56	8.70	6.96	7.88
Al_2O_3	16.99	17.88	15.92	18.21	18.61
SiO_2	34.54	31.79	34.82	32.05	33.47
CaO	25.37	25.26	25.27	24.86	25.08
TiO_2^{tot}	15.28	17.92	16.19	18.98	15.12
Sc_2O_3	0.37	0.41	BLD	0.24	0.13
V_2O_3	0.39	0.35	0.19	0.19	0.32
Ti_2O_3	9.16	9.64	9.40	11.82	8.23
TiO_2	5.37	7.56	6.01	6.04	6.16
TOTAL	100.37	100.45	100.31	100.37	99.88
Cations per six O anions					
Si	1.314	1.219	1.324	1.224	1.273
^{IV}Al	0.686	0.781	0.676	0.776	0.727
Tet. sum	2.000	2.000	2.000	2.000	2.000
^{VI}Al	0.075	0.027	0.037	0.044	0.107
Mg	0.464	0.432	0.493	0.396	0.447
Ca	1.000	1.000	1.000	1.000	1.000
Sc	0.012	0.014	0.000	0.008	0.004
V	0.011	0.010	0.005	0.006	0.009
Ti^{3+}	0.286	0.303	0.294	0.373	0.258
Ti^{4+}	0.151	0.214	0.169	0.172	0.174
Oct. Sum	1.999	2.000	1.998	1.999	1.999

References: 1, 2 = Isolated grains in palisade body. 3–5 = Adjacent to spinel. BLD = Below limit of detection of electron microprobe of 0.044 wt% Sc_2O_3. FeO was measured and was below the detection limit of 0.041 wt% in all cases. Analyses are normalized to four cations, including two tetrahedral cations and one Ca cation, per six O anions according to the methods of Beckett (1986).

TABLE 2. Analyses of perovskite in TS2.

	1	2	3	4
Al_2O_3	0.67	0.58	0.15	0.22
SiO_2	0.03	0.04	0.20	0.20
CaO	39.86	39.52	41.49	41.05
TiO_2	51.34	52.77	58.38	57.94
V_2O_3	0.31	0.28	0.17	0.17
Nb_2O_5	7.95	5.39	0.08	0.12
Ta_2O_5	0.21	0.82	BLD	BLD
Total	100.37	99.40	100.47	99.70
Cations per three O anions				
Al	0.018	0.016	0.004	0.006
Si	0.001	0.001	0.016	0.004
Ca	0.981	0.978	1.001	0.997
Ti	0.886	0.917	0.988	0.998
V	0.006	0.005	0.003	0.003
Nb	0.083	0.056	0.006	0.001
Ta	0.001	0.005	0	0
Total cations	1.976	1.978	2.018	2.009

References: 1, 2 = Nb-rich perovskite. 3 = Rim of Nb-rich pv. 4 = Typical, uniform, isolated grain.
BLD = Below limit of detection of electron microprobe of 0.143 wt% Ta_2O_5. In all cases, FeO is below the detection limit of 0.044 wt%.

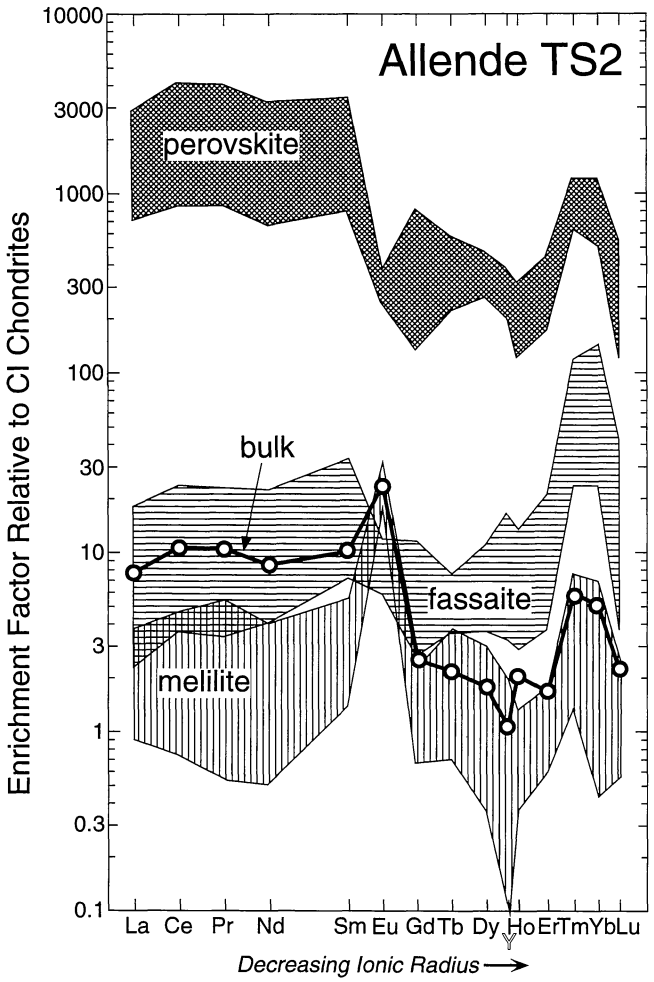

FIG. 9. Ranges of chondrite-normalized REE abundances in melilite, fassaite, and perovskite in TS2 and a calculated bulk pattern. Note the Group II-like overprint on all patterns. The bulk pattern was calculated from the averages of 8 melilite, 6 fassaite, and 17 perovskite analyses and the modal abundances of the phases.

respectively. The bulk REE pattern, also shown in Fig. 9, is dominated by that of melilite despite the high REE contents of perovskite. The bulk pattern appears to be related to the Group II patterns commonly found in Allende fine-grained inclusions (*e.g.*, Martin and Mason, 1974). This type of pattern, in which there is a negative Eu anomaly and the refractory heavy REE (HREE), Gd through Er, are strongly depleted relative to the other REE, is relatively rare in coarse-grained inclusions. Unlike normal Group II patterns, the bulk pattern of TS2 has a positive Eu anomaly, and Yb is only slightly, rather than strongly, depleted relative to the light REE (LREE). The analyses, which include coarse perovskite and fassaite from throughout the inclusion and melilite from each of the three major petrographic regimes (patchy melilite; melilite in the outer ~500 μm of the inclusion; and the palisade body) show that each phase exhibits patterns that show the effects of the normal crystal-chemical preferences of that phase upon the Group II-like bulk pattern. As a result, fassaite, which favors HREE over LREE, has nearly flat patterns, and perovskite, which favors LREE, has chondrite-normalized LREE abundances much greater than those of the HREE.

TABLE 3. Representative ion probe analyses of melilite, fassaite and perovskite in TS2. Results in parts per million unless otherwise indicated. Uncertainties are $\pm 1\sigma$ and upper limits are $<2\sigma$, based on counting statistics. Uncertainties are given only where they exceed 5% (relative).

	1	2	3	4	5	6
Phase	Mel, $Åk_{19}$	Mel, $Åk_{31}$	Mel, $Åk_{41}$	Pv	Pv	Fass
MgO (%)	2.43	4.15	5.64	0.02	0.04	7.01
Al_2O_3 (%)	28.96	24.56	20.61	0.15	0.22	16.54
SiO_2 (%)	25.92	28.53	30.79	0.16	0.15	35.89
CaO (%)	42.45	42.64	42.83	43.14	40.77	25.36
TiO_2 (%)	0.03	0.04	0.03	56.17	58.08	14.51
Li	0.036 ± 0.007	0.070 ± 0.012	0.100 ± 0.014	<0.11	0.025 ± 0.009	<0.038
Be	0.945 ± 0.038	0.459 ± 0.031	0.453 ± 0.031	<0.18	<0.0061	0.208 ± 0.066
B	0.598 ± 0.066	0.564 ± 0.073	1.17 ± 0.11	<0.48	0.125 ± 0.042	1.66 ± 0.31
F	11.4 ± 5.1	<9.8	<9.0	69 ± 34	27 ± 11	19.8 ± 8.9
Na	99.8	64.1	33.9	16.8 ± 1.6	19.7	181
P	13.4 ± 6.4	<14	<16	<7.5	<2.8	29.4 ± 5.1
Cl	43 ± 13	39 ± 14	91 ± 22	—	<20	—
K	9.51 ± 0.58	9.63 ± 0.64	14.6 ± 0.8	14.9 ± 2.0	12.9 ± 0.9	60.8
Sc	<2.4	3.1 ± 1.4	<2.8	110	41.0	1985
Ti	196	219	209			
V	15.3 ± 4.1	15.2 ± 5.9	<12.9	204	185	1393
Cr	10.0 ± 1.6	18.4 ± 2.4	17.2 ± 2.7	19.0 ± 2.5	36.5 ± 2.0	157 ± 10
Mn	26 ± 13	27 ± 12	<22	<1.34	1.5 ± 0.33	<31
Fe	1066 ± 74	211 ± 67	299 ± 73	726 ± 141	1438 ± 87	383 ± 114
Co	10.8 ± 2.1	6.8 ± 2.3	<4.0	<9.2	21.7 ± 3.7	<4.5
Rb	0.65 ± 0.26	0.47 ± 0.29	<0.56	<3.8	<0.50	4.18 ± 0.68
Sr	229	250	237	309 ± 36	449	85.2
Y	1.12 ± 0.09	0.641 ± 0.074	0.223 ± 0.045	81.6 ± 3.7	128.4	7.76 ± 0.40
Zr	0.214 ± 0.062	0.178 ± 0.063	0.215 ± 0.072	134 ± 9	109	292
Nb	0.056 ± 0.028	0.282 ± 0.070	0.113 ± 0.046	120	292.6	2.12 ± 0.30
Cs	0.139 ± 0.069	0.56 ± 0.16	<0.091	<0.74	1.55 ± 0.31	<0.17
Ba	49.6	60.8	60.6	13.6 ± 1.7	27.2	22.1
La	0.913 ± 0.055	0.705 ± 0.054	2.71 ± 0.034	112	312	0.540 ± 0.053
Ce	2.39 ± 0.14	1.46 ± 0.13	1.22 ± 0.12	406	1243	2.17 ± 0.17
Pr	0.410 ± 0.072	0.335 ± 0.073	0.084 ± 0.037	55.9	174	0.303 ± 0.083
Nd	1.78 ± 0.35	1.32 ± 0.33	0.62 ± 0.24	230	684	1.83 ± 0.33
Sm	0.77 ± 0.16	0.43 ± 0.17	0.41 ± 0.16	87.3	243	1.05 ± 0.11
Eu	1.74 ± 0.13	1.83 ± 0.15	1.23 ± 012	5.09 ± 0.29	5.05 ± 0.32	0.371 ± 0.045
Gd	<0.37	<0.30	<0.20	20.0 ± 4.6	15.0 ± 7.4	0.52 ± 0.21
Tb	<0.051	<0.062	<0.042	3.42 ± 0.79	2.7 ± 1.0	0.13 ± 0.047
Dy	<0.210	0.34 ± 0.12	0.160 ± 0.075	17.7 ± 2.1	29.7 ± 2.4	0.88 ± 0.16
Ho	0.055 ± 0.026	0.258 ± 0.052	0.074 ± 0.029	2.34 ± 0.55	4.18 ± 0.53	0.298 ± 0.068
Er	<0.142	0.251 ± 0.081	<0.095	7.8 ±1.2	9.6 ± 2.5	0.59 ± 0.10
Tm	<0.051	0.073 ± 0.035	0.052 ± 0.025	7.42 ± 0.46	9.62	0.568 ± 0.061
Yb	0.605 ± 0.092	0.325 ± 0.075	0.091 ± 0.039	51.9	71.5	3.85 ± 0.29
Lu	0.046 ± 0.016	0.043 ± 0.020	<0.021	0.59 ± 0.34	3.92 ± 0.67	0.093 ± 0.034
Hf	<0.27	<0.39	<0.24	2.50 ± 0.90	3.5 ± 1.7	6.87 ± 0.33
Pb	<0.84	<0.60	<0.60	11.5 ± 5.0	23.5 ± 3.1	5.9 ± 1.6
Th	0.191 ± 0.095	0.59 ± 0.19	0.47 ± 0.17	1.86 ± 0.33	39.9 ± 1.8	<0.046
U	0.077 ± 0.024	<0.034	0.076 ± 0.027	1.6 ± 0.31	4.62 ± 0.24	<0.026

In this inclusion, melilite encloses many fine perovskite and fassaite grains, and it is difficult to obtain ion probe analyses that are uncontaminated by these inclusions. Because of this, plots of Ti and trivalent REE abundances *vs.* $X_{Åk}$ show a great deal of scatter when all analyses are plotted. A subset of nine analyses, however, appears to define a fairly uniform lower limit of 200–220 ppm Ti. We take these values to be true Ti contents of melilite, and we assume these analyses to be free of inclusions. When trace element abundances from these analyses are plotted as a function of $X_{Åk}$ (Fig. 10), coherent trends, rather than scatter, are observed, as in the plot of La abundances (Fig. 10a). This plot shows that La contents decrease with increasing $X_{Åk}$. This may reflect the fact that, for the trivalent REE, melilite/liquid Ds decrease as $X_{Åk}$ increases, as was found in experiments on Type B inclusion melts (Kuehner *et al.*, 1989; Beckett *et al.*, 1990; Davis *et al.*, 1996). The results of these experiments give rise to fractional crystallization models that predict inverse relationships between $X_{Åk}$ and La contents of melilite in the mantles of Type B1 inclusions, but such trends are commonly not observed (*e.g.*, Davis *et al.*, 1992; Kennedy *et al.*, 1997). Ironically, for TS2, an inverse trend is observed but not predicted. We attempted to model the La contents of TS2 melilite by assuming: that a linear relationship existed between melilite composition and F, the fraction of liquid remaining; that melilite began crystallizing with a composition of $Åk_9$, reaching $Åk_{65}$ when $F = 2\%$; and that the melilite/liquid D variation with melilite and liquid composition was the same as in Type B melts. The resulting Rayleigh fractionation model, based

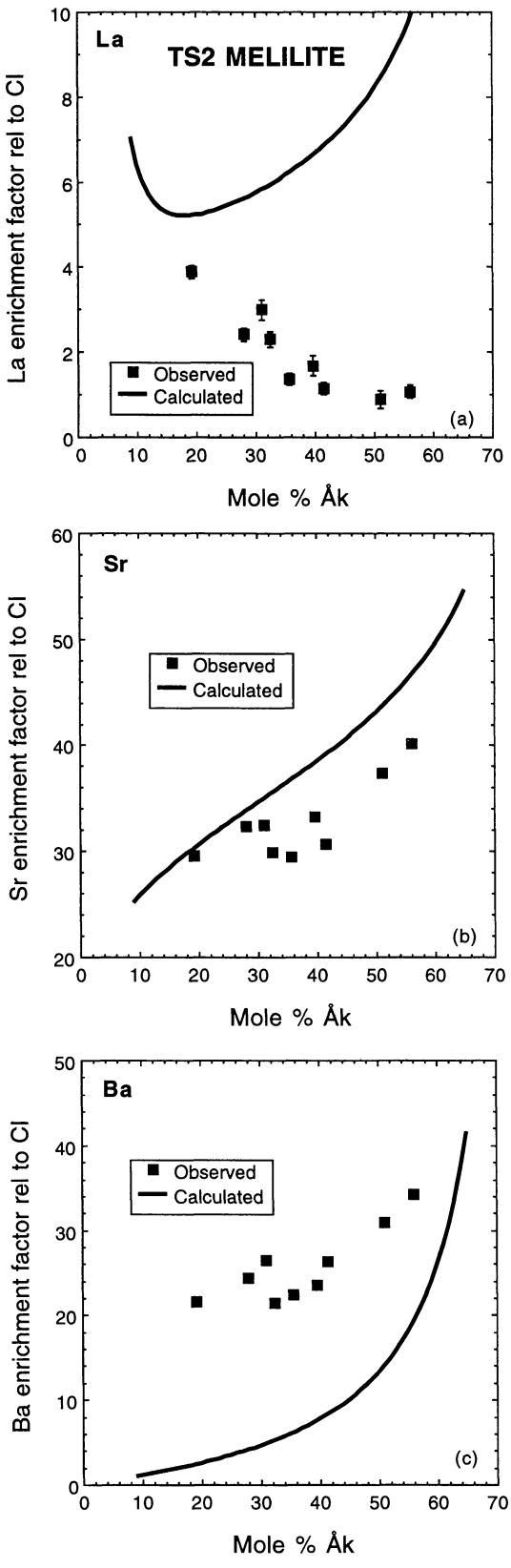

FIG. 10. Plots of chondrite-normalized La (a), Sr (b), and Ba (c) abundances *vs.* mol% Åk in inclusion-free ion probe analyses of melilite. Also shown are calculated Rayleigh fractionation curves. The analyses have uncertainties of ~3 mol% Åk.

on the calculated bulk La content of 7.4 × CI chondrites, is shown as a curve in Fig. 10a. The model predicts a decrease in La contents with $X_{Åk}$ in early melilite, but melilite represents such a high proportion of the inclusion that by the time it reaches $Åk_{25}$ in composition, the melt becomes sufficiently fractionated that reservoir effects dominate and La contents begin to increase with $X_{Åk}$.

Better results are obtained for Sr (Fig. 10b), using the same *F* *vs.* $X_{Åk}$ relationship as above, the calculated bulk content of 31.2 × CI, and a constant D of 0.8 (Kuehner *et al.*, 1989). The abundances of Sr are predicted to increase with $X_{Åk}$ in the model, and this is observed in the data. An analogous calculation for Ba, using a constant D of 0.04 (Beckett *et al.*, 1990) and the calculated bulk content of 24.3 × CI does not work well, as the observed Ba contents are much higher than those predicted (Fig. 10c). This is also the case for attempts to model the Ba contents of mantle melilite in Type B1 inclusions (Davis *et al.*, 1992; Simon *et al.*, 1996; Kennedy *et al.*, 1997). In Type B1 inclusions and in the present sample, the partitioning of the REE and Ba into melilite is not understood and requires further study.

The light REE are compatible in perovskite (Kennedy *et al.*, 1994) and are positively correlated with Nb, as shown by a plot of Nb *vs.* La (Fig. 11). The analyses of coarse-grained perovskite from the palisade body and from elsewhere in the inclusion fall along a single trend, which indicates that the palisade body and the host inclusion followed similar liquid lines of descent. In addition, the slopes of the REE patterns of perovskite decrease, becoming less LREE-enriched, with decreasing overall REE content, which is also consistent with fractional crystallization.

All of the analyzed perovskite grains have superchondritic Y/Zr ratios, probably reflecting the bulk undersampling of the ultrarefractory elements that is characteristic of Group II CAIs. The extremely Nb-rich grains were not analyzed by ion probe in order to preserve them for a future search for excess ^{92}Zr from the decay of ^{92}Nb ($T_{1/2}$ = 3.6 × 10^7 year). Trace element abundances in the fine-grained perovskite could not be determined either because the grains are much too fine and sparse (*e.g.*, Fig. 3b) to constitute a significant

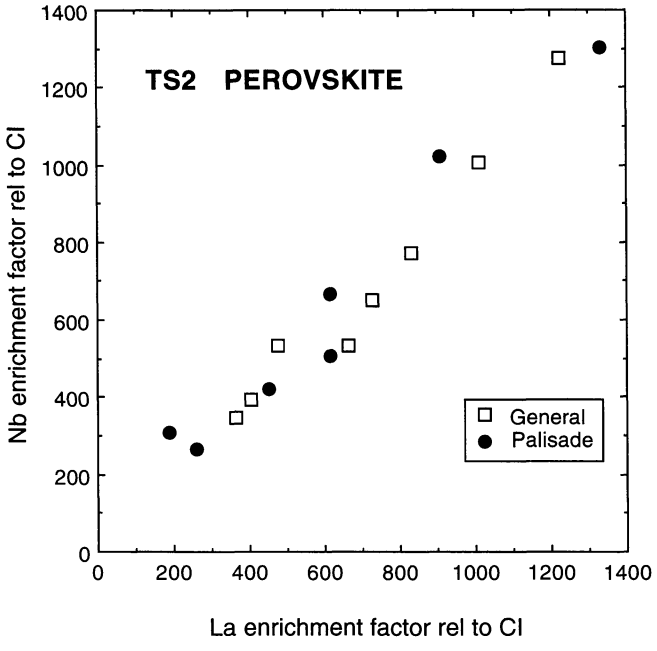

FIG. 11. Plot of Nb *vs.* La in perovskite.

proportion of the analytical volume of an ion probe spot, or they are too trace element-poor to be detected. Melilite analyses with elevated Ti contents do not have higher La or Nb contents than those with low Ti contents.

DISCUSSION

Any model for the formation of TS2 must account for its unusual features: the bimodal size distribution of spinel; the patchy zoning of melilite; and the ubiquitous Group II-like overprint on the chondrite-normalized REE patterns. The latter observation essentially rules out incorporation of unrelated xenoliths, xenocrysts, or additional liquids as explanations for the patchy zoning of the melilite, because the trace element data indicate a single source for all components of the inclusion. This strongly suggests that the unusual texture reflects an unusual thermal history. The most plausible model to account for the observed features of TS2 is the following. (1) Precursors that have a modified Group II chondrite-normalized REE pattern melt. (Discussions of the gas/solid fractionation events that led to Group II patterns have been presented previously, *e.g.*, Davis and Grossman, 1979.) Although Group II patterns are most commonly found in fine-grained inclusions, TS2 is too melilite-rich and spinel-poor to be simply a melted fine-grained inclusion. (2) Nebular gas that was present between the precursor grains is trapped by the melt, forming bubbles. (3) Melilite crystals nucleate and grow rapidly due to fast cooling and/or supercooling. The rapid growth causes melilite to be dendritic, to trap pockets of melt, and to be enriched in spinel components and TiO_2. (4) Crystallization slows. Coarse spinel grows and collects against bubbles, forming spherical shells. Additional spinel grains form clumps and chains. After the growth of the dendritic melilite, relatively Åk-rich melilite crystallizes from the melt trapped in pockets and between arms of dendrites, and takes on the optical orientations of the host crystals. Coarse spinel becomes enclosed in Åk-rich melilite. (5) Bubbles coalesce and break, filling with late-stage melt. The shape of one large bubble was preserved by the spinel shell of the palisade body. (6) Slow cooling or reheating allows early melilite to become stoichiometric by exsolving fine grains of spinel, perovskite, and fassaite.

Evidence for crystallization of this inclusion from a melt is quite strong. Chains, sheets and rings of spinel like those found in TS2 are also commonly observed in synthetic run products from experiments on CAI melts (*e.g.*, Stolper and Paque, 1986). The presence of a palisade body also supports a molten origin. The formation of palisade bodies was discussed by Simon and Grossman (1997). According to their model, the curved boundary of the palisade body probably originated as a melt/vapor bubble contact upon which spinel grains nucleated and/or collected against. Eventually, the bubble broke and filled with fractionated melt, and the spinel shell around the bubble preserved its shape.

Other features of this inclusion are consistent with an early episode of rapid crystallization. In experiments conducted in air on melts with the bulk composition of an average Type B inclusion (Stolper and Paque, 1986; Simon *et al.*, 1996), runs cooled at ~50–100 °C/h typically yield large, weakly or irregularly zoned, dendritic melilite crystals that contain melt pockets. Examples are shown in Fig. 12. This morphology is diagnostic of rapid crystal growth (J. Paque, pers. comm.), which may be due to rapid cooling and/or to supercooling. Like the synthetic crystals, the relatively aluminous, spinel-bearing melilite crystals in TS2 have no systematic core-rim or lengthwise zoning and have highly irregular shapes. Note the similarity between the synthetic dendritic melilite crystals in Fig. 12 and

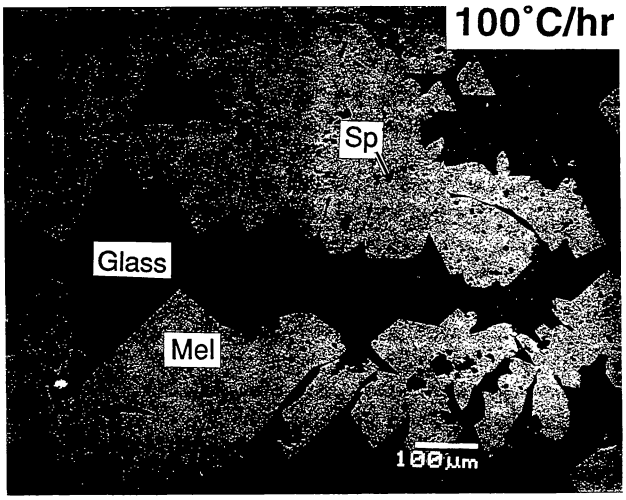

FIG. 12. Backscattered electron image of dendritic melilite in a run product cooled at 100 °C/h. Note melt pockets enclosed in melilite and interfingering of melt and branches of the dendrites. Abbreviations as used previously.

the shapes of the aluminous melilite in Fig. 3c, especially the one along the top of the image. Initial crystallization of the aluminous melilite as dendritic crystals could account for the unusual intergrowth patterns observed in TS2.

After the growth of these crystals, crystal growth slowed. Liquid that was trapped in pockets and between arms of the dendritic melilite crystallized to relatively magnesian melilite and took on the optical orientation of the host (or adjacent) crystal, forming the Åk-rich patches. The Åk-poor melilite preserved the original, dendritic shapes of the crystals. In some cases, the trapped melt continued to fractionate to the point where fassaite or perovskite crystallized, accounting for the occurrence of these phases enclosed in the centers of some of the patches of Mg-rich melilite.

The numerous tiny inclusions of spinel, fassaite and perovskite found in the relatively Al-rich regions of patchy melilite probably formed by exsolution and are also consistent with an episode of rapid crystal growth. There are several reasons why it is unlikely that these grains were simply trapped during the growth of their host melilite crystals. First, the fine spinel grains are dispersed throughout the melilite, rather than occurring in clumps and chains, as might be expected if they had been incorporated by random capture during growth. Second, crystallization of perovskite and fassaite from a melilite-rich composition like that of TS2 requires a great deal of prior crystallization of melilite in order to increase the concentration of TiO_2 in the residual melt; perovskite and fassaite should not be available for incorporation into early melilite. Finally, it is unlikely that the grains are small due to reaction with melilite. There do not appear to be any reaction rims around the spinels or sharp gradients in the compositions of the melilite adjacent to them that would indicate that the spinel and melilite were reacting with each other. Our best explanation for the occurrence of fine spinel, perovskite, and fassaite in aluminous melilite is that the early melilite crystallized so rapidly that it was originally somewhat nonstoichiometric, and the grains exsolved from it during a period of relatively slow cooling. Melilite could have incorporated excess spinel components (MgO and Al_2O_3) and TiO_2 during rapid growth, which were later exsolved in the form of spinel, fassaite, and perovskite. There are some rocks in which minerals contain even denser concentrations of fine inclusions

than does the melilite described herein. In one example, exsolution is thought to account for the clouding of plagioclase in some metadolerites (Armbrustmacher and Banks, 1974). In addition, pyroxene and plagioclase grains in some eucrites, including Juvinas and Stannern, are densely clouded with fine inclusions of ilmenite, chromite, metal, and troilite. As in the model we propose for TS2, these grains are thought to have formed when excess components that were incorporated during rapid crystallization of the host rock exsolved during slow cooling (Harlow and Klimentidis, 1980). These authors reject the trapped-crystal hypothesis for several reasons. One point is that an unreasonably high nucleation density would be required for the included phases. Also, they assume the crystals would have been trapped with melt, and they found no evidence for this.

Nonstoichiometry of melilite, however, has not been reported, either from natural samples or synthetic melilite, even in run products cooled at 1000 °C/h (*e.g.*, Stolper and Paque, 1986). Phase abundance measurements from digital BSE images of several areas show that there is ~5 vol% spinel, 1% fassaite, and 0.05% perovskite in the spinel-rich zones. In order to determine what the preexsolution compositions of the early melilite would have been, we analyzed six areas of melilite rich in fine inclusions with an electron beam defocused to a diameter of ~50 μm. Representative defocused-beam analyses (DBAs) are given in Table 4 along with spot analyses of the melilite within them. The DBAs appear to have sampled ~90% melilite and 10% spinel. This may seem like a large degree of exsolution to invoke, but it is probably less than that indicated by the densely clouded grains discussed above.

Each DBA has a higher MgO content than the melilite composition that would be consistent with its Al_2O_3 and SiO_2 contents. For example, the Al_2O_3 and SiO_2 contents of DBA1 both correspond to a composition of ~$Åk_{32}$, but its MgO content of 9.56 wt% is found in $Åk_{64}$. Compared to the melilite they contain, the DBAs have higher MgO, Al_2O_3 and TiO_2 and lower SiO_2 and CaO contents. The DBAs have lower Åk contents based on their Al and Si abundances, and higher Åk contents based on their Mg abundances, than the melilite in them. All six analyses have 25–26 wt% Al_2O_3 and 28–29 wt% SiO_2, with somewhat wider ranges of MgO (7.0–9.6 wt%) and CaO. Another argument against random capture of the fine spinel is that it probably would have led to greater variability among the DBAs than is observed unless the fine spinel grains were homogeneously dispersed throughout the melt.

Beckett (1986) performed isothermal crystallization experiments on a composition that very closely approximates his calculated bulk composition of TS2 (ignoring alteration products). He found that the equilibrium crystallization sequence consisted of melilite first, followed closely (within 15 °C) by spinel, with perovskite coming in very late. He also found that melilite compositions ranged from $Åk_1$ to $Åk_{36}$, which are generally more gehlenitic and correspond to higher crystallization temperatures than most of the melilite compositions found in TS2. Our data and observations for TS2 can be interpreted, therefore, as the result of suppression of crystallization due to rapid cooling, an effect which has been well documented experimentally (MacPherson *et al.*, 1984; Stolper and Paque, 1986). This would explain why, when melilite began to crystallize in TS2, it did so with a composition more Åk-rich than that of the initial melilite of the equilibrium experiments. Perhaps spinel failed to nucleate at its equilibrium crystallization temperature, causing the melt and the melilite itself to become oversaturated in the spinel component. Although the DBAs have higher MgO abundances than does the melilite they contain, Table 4 shows that the Åk contents (based on Al and Si) of the final melilite are higher than those of the DBAs, which suggests that the exsolution was driven in part by equilibration to higher Åk values at temperatures lower than those at which the initial crystallization took place.

According to our model, the coarse spinel grains mostly grew during a period of slow cooling, after the crystallization of the dendritic melilite. This would explain why they occur in relatively magnesian melilite and would also account for the lack of fine spinel in the immediate vicinity of coarse spinel, since this late melilite, which grew slowly, would not be expected to have exsolved fine spinel. We detect no overgrowths or reaction rims on the coarse spinel to suggest multiple episodes of spinel growth. The similarity in composition between the coarse and fine spinels (Fig. 8) indicates that they are somehow related and that the coarse grains are not exotic to the inclusion. Based on reports of V-rich spinel in CAIs (*e.g.*, Armstrong *et al.*, 1985), V probably is compatible in spinel. The relatively V-rich coarse spinel grains in TS2 probably crystallized earlier than the coarse spinel grains with lower V_2O_3 contents.

TABLE 4. Defocused beam analyses of spinel-bearing melilite and point analyses of the melilite in those areas.

	DBA1	mel in DBA1	DBA2	mel in DBA2	DBA3	mel in DBA3
MgO	9.56	6.17	8.34	6.47	8.44	6.41
Al_2O_3	25.28	21.36	25.58	21.07	25.49	20.65
SiO_2	29.05	31.34	28.15	30.39	29.00	31.07
CaO	35.93	42.12	37.04	41.38	37.43	41.65
TiO_2	0.42	0.04	0.17	0.04	0.25	0.04
TOTAL	100.24	101.03	99.28	99.35	100.61	99.82
Cations per seven O anions						
Mg	0.639	0.416	0.566	0.444	0.564	0.438
Al	1.335	1.138	1.371	1.143	1.347	1.114
Si	1.302	1.417	1.280	1.399	1.300	1.422
Ca	1.725	2.040	1.805	2.041	1.798	2.043
Ti	0.014	0.001	0.006	0.001	0.008	0.001
Total cations	5.015	5.012	5.028	5.028	5.017	5.018
Åk (Mg)	64	42	57	44	56	44
Åk (Al)	33	43	31	43	33	44
Åk (Si)	30	42	28	40	30	42

Another feature of TS2 that we must account for is the straight melilite grain boundaries, which require that the dendritic shapes of the early crystals were not propagated by the late overgrowths. It is possible that the period of slow cooling that allowed the aluminous melilite to undergo exsolution also allowed the overgrowths to form straight grain boundaries. There are no experimental observations that would indicate whether contacts between overgrowths on dendritic crystals would tend to be straight or mimic the irregularly shaped cores.

CONCLUDING STATEMENTS

Herein we have presented evidence that TS2 contains rapidly grown melilite enclosed in more slowly grown melilite. The observations reported here expand the known range of textures of and, possibly, cooling rates experienced by once-molten, coarse-grained inclusions. If the rapid growth was due to fast cooling, and if results from dendrite-producing experiments on Type B compositions are applicable, rates from ~50 to ~100 °C/h are implied. These rates, the first such estimates for a natural CTA (albeit an unusual one), are somewhat higher than those inferred for Type B1 inclusions, 2–50 °C/h, based on experimentally reproduced reverse zoning in melilite due to suppression of anorthite crystallization (MacPherson *et al.*, 1984), and from the similarity of the morphologies of natural melilite crystals to those grown at cooling rates within that range (Stolper and Paque, 1986). Very little experimental work has been done on Type A inclusion compositions, however. Equilibrium crystallization sequences have been determined (Paque and Stolper, 1984; Beckett, 1986), but variations of texture with cooling rate are not well known.

Teshima and Wasserburg (1985) concluded from petrographic characteristics of CTAs that they had been modified by recrystallization during metamorphism. Perhaps CTAs in general cooled more quickly than B1s and contain rapidly grown melilite that has been recrystallized, obscuring primary crystallization features. The cooling rate estimates given here for TS2 probably apply to higher temperatures than those for Type B CAIs. The differences between the cooling rates inferred here for TS2 and those for Type Bs may reflect, therefore, different parts of similar histories, with relatively rapid cooling at high temperatures and slower cooling at low temperatures. Alternatively, TS2 may have had an anomalously high cooling rate early in its history. We favor the latter explanation, because otherwise the unusual features observed in TS2 and reported in this paper would be common among CTAs.

In our continuing studies of CTAs, we will attempt to identify primary crystallization features in order to obtain a better understanding of the cooling histories of these inclusions. Although the inference of cooling rates from textures of CTAs might not be as straightforward as for B1s, additional experiments on Type A compositions should be performed to make our estimates as accurate as possible.

Acknowledgments–We are grateful to F. M. Richter for allowing free access to his experimental run products, to I. M. Steele for assistance with cathodoluminescence imaging, and to G. J. MacPherson and J. M. Paque for helpful discussions. Reviews by J. R. Beckett and an anonymous reviewer contained some thought-provoking comments and led to improvements in the text. This work was supported by the National Aeronautics and Space Administration through grants NAGW-3340 and NAG5-4476 (LG), NAGW-3384 and NAG5-4298 (AMD), and NAGW-3345 (to R. N. Clayton), and funding is gratefully acknowledged.

Editorial handling: S. R. Taylor

REFERENCES

ARMBRUSTMACHER T. J. AND BANKS N. G. (1974) Clouded plagioclase in metadolerite dikes, southeastern Bighorn Mountains, Wyoming. *Am. Mineral.* **59,** 656–665.

ARMSTRONG J. T., EL GORESY A. AND WASSERBURG G. J. (1985) A prize noble Ur-Fremdling – Its history and implications for the formation of Fremdlinge and CAI. *Geochim. Cosmochim. Acta* **49,** 1001–1022.

BECKETT J. R. (1986) The origin of calcium-, aluminum-rich inclusions from carbonaceous chondrites: An experimental study. Ph.D. thesis, The University of Chicago. 373 pp.

BECKETT J. R. AND STOLPER E. (1994) The partitioning of Na between melilite and liquid: An experimental study with applications to Type B CAIs (abstract). *Lunar Planet. Sci.* **25,** 79–80.

BECKETT J. R., SPIVACK A. J., HUTCHEON I. D., WASSERBURG G. J. AND STOLPER E. M. (1990) Crystal chemical effects on the partitioning of trace elements between mineral and melt: An experimental study of melilite with applications to refractory inclusions from carbonaceous chondrites. *Geochim. Cosmochim. Acta* **54,** 1755–1774.

DAVIS A. M. AND GROSSMAN L. (1979) Condensation and fractionation of rare earths in the solar nebula. *Geochim. Cosmochim. Acta* **43,** 1611–1632.

DAVIS A. M., SIMON S. B. AND GROSSMAN L. (1990) Trace element distributions in Allende compact type a inclusions (abstract). *Meteoritics* **25,** 356.

DAVIS A. M., SIMON S. B. AND GROSSMAN L. (1992) Melilite composition trends during crystallization of Allende Type B1 refractory inclusion melts (abstract). *Lunar Planet. Sci.* **23,** 281–282.

DAVIS A. M., RICHTER F. M., SIMON S. B. AND GROSSMAN L. (1996) The effect of cooling rate on melilite/liquid partition coefficients for Y and REE in Type B CAI melts (abstract). *Lunar Planet. Sci.* **25,** 79–80.

EL GORESY A., NAGEL K. AND RAMDOHR P. (1977) Type A Ca-, Al-rich inclusions in Allende meteorite: Origin of the perovskite-fassaite symplectite around rhönite and chemistry and assemblages of the refractory metals (Mo, W) and platinum metals (Ru, Os, Ir, Re, Rh, Pt) (abstract). *Meteoritics* **12,** 216.

FAHEY A. J., ZINNER E. K., CROZAZ G. AND KORNACKI A. S. (1987) Microdistributions of Mg isotopes and REE abundances in a Type A calcium-aluminum-rich inclusion from Efremovka. *Geochim. Cosmochim. Acta* **51,** 3215–3229.

FUCHS L. H. (1971) Occurrence of wollastonite, rhönite, and andradite in the Allende meteorite. *Am. Mineral.* **56,** 2053–2068.

GROSSMAN L. (1975) Petrography and mineral chemistry of Ca-rich inclusions in the Allende meteorite. *Geochim. Cosmochim. Acta* **39,** 433–454.

GROSSMAN L. (1980) Refractory inclusions in the Allende meteorite. *Ann. Rev. Earth Planet. Sci.* **8,** 559–608.

HAGGERTY S. E. (1976) Titanium cosmothermometry and rhönite decomposition in Allende (abstract). *Meteoritics* **11,** 295.

HARLOW G. E. AND KLIMENTIDIS R. (1980) Clouding of pyroxene and plagioclase in eucrites: Implications for post-crystallization processing. *Proc. Lunar Planet. Sci. Conf.* **11th,** 1131–1143.

KENNEDY A. K., LOFGREN G. E. AND WASSERBURG G. J. (1994) Trace-element partition coefficients for perovskite and hibonite in meteorite compositions. *Chem. Geol.* **117,** 379–390.

KENNEDY A. K., BECKETT J. R., EDWARDS D. A. AND HUTCHEON I. D. (1997) Trace element disequilibria and magnesium isotope heterogeneity in 3655A: Evidence for a complex multi-stage evolution of a typical Allende Type B1 CAI. *Geochim. Cosmochim. Acta* **61,** 1541–1561.

KUEHNER S. M., LAUGHLIN J. R., GROSSMAN L., JOHNSON M. L. AND BURNETT D. S. (1989) Determination of trace element mineral/liquid partition coefficients in melilite and diopside by ion and electron microprobe techniques. *Geochim. Cosmochim. Acta* **53,** 3115–3130.

MACPHERSON G. J. AND DAVIS A. M. (1993) A petrologic and ion microprobe study of a Vigarano Type B refractory inclusion: Evolution by multiple stages of alteration and melting. *Geochim. Cosmochim. Acta* **57,** 231–243.

MACPHERSON G. J. AND DAVIS A. M. (1994) Refractory inclusions in the prototypical CM chondrite, Mighei. *Geochim. Cosmochim. Acta* **58,** 5599–5625.

MACPHERSON G. J. AND GROSSMAN L. (1979) Melted and non-melted coarse-grained Ca-, Al-rich inclusions in Allende (abstract). *Meteoritics* **14,** 479–480.

MACPHERSON G. J. AND GROSSMAN L. (1984) "Fluffy" Type A Ca-, Al-rich inclusions in the Allende meteorite. *Geochim. Cosmochim. Acta* **48,** 29–46.

MACPHERSON G. J., PAQUE J. M., STOLPER E. AND GROSSMAN L. (1984) The origin and significance of reverse zoning in melilite from Allende Type B inclusions. *J. Geol.* **92,** 289–305.

MARTIN P. M. AND MASON B. (1974) Major and trace elements in the Allende meteorite. *Nature* **249,** 333–334.

MITCHELL R. H. (1996) Perovskites: A revised classification scheme for an important rare earth element host in alkaline rocks. In *Rare Earth Minerals: Chemistry, Origin and Ore Deposits* (eds. A. P. Jones, F. Wall and C. T. Williams), pp. 41–76. Chapman & Hall, London, U.K.

PAQUE J. M. AND STOLPER E. (1984) Crystallization experiments on a range of Ca-Al-rich inclusion compositions (abstract). *Lunar Planet. Sci.* **15,** 631–632.

POUCHOU J. L. AND PICHOIR F. (1984) A new model for quantitative x-ray microanalysis. Part I: Application to the analysis of homogeneous samples. *Rech. Aerosp.* **3,** 13–38.

SIMON S. B. AND GROSSMAN L. (1997) *In situ* formation of palisade bodies in calcium-, aluminum-rich refractory inclusions. *Meteorit. Planet. Sci.* **32,** 61–70.

SIMON S. B., GROSSMAN L. AND DAVIS A. M. (1991) Fassaite composition trends during crystallization of Allende Type B refractory inclusion melts. *Geochim. Cosmochim. Acta* **55,** 2635–2655.

SIMON S. B., DAVIS A. M. AND GROSSMAN L. (1995) Crystallization of compact Type A refractory inclusions: Implications from crystal zoning and trace element distribution (abstract). *Lunar Planet. Sci.* **26,** 1303–1304.

SIMON S. B., DAVIS A. M., RICHTER F. M., AND GROSSMAN L. (1996) Experimental investigation of the effect of cooling rate on melilite/liquid distribution coefficients for Sr, Ba, and Ti in Type B refractory inclusion melts (abstract). *Lunar Planet. Sci.* **27,** 1201–1202.

SIMON S. B., DAVIS A. M. AND GROSSMAN L. (1997) Evidence for rapid growth of melilite in an unusual compact Type A refractory inclusion from Allende (abstract). *Lunar Planet. Sci.* **28,** 1317–1318.

STOLPER E. AND PAQUE J. M. (1986) Crystallization sequences of Ca-Al-rich inclusions from Allende: The effects of cooling rate and maximum temperature. *Geochim. Cosmochim. Acta* **50,** 1785–1806.

TESHIMA J. AND WASSERBURG G. J. (1985) Textures, metamorphism and origin of Type A CAI's (abstract). *Lunar Planet. Sci.* **16,** 855–856.